Real-time Identification and Tuning of Multirotors Based on Deep Neural Networks for Accurate Trajectory Tracking Under Wind Disturbances

AbdulAziz Y. AlKayas[a,b,*], Mohamad Chehadeh[a,*], Abdulla Ayyad[a] and Yahya Zweiri[a,c,d]

[a]Khalifa University Center for Autonomous Robotic Systems (KUCARS), Khalifa University, Abu Dhabi, United Arab Emirates
[b]Mechanical Engineering Department, Khalifa University, Abu Dhabi, United Arab Emirates
[c]Aerospace Engineering Department, Khalifa University, Abu Dhabi, United Arab Emirates
[d]Faculty of Science, Engineering and Computing, Kingston University London, London, SW15 3DW, UK

arXiv:2106.03459v1 [cs.RO] 7 Jun 2021

ARTICLE INFO

Keywords:
Unmanned Aerial Vehicles
System Identification
Adaptive and Robust Control
Trajectory Tracking
PID Control
Deep Learning

ABSTRACT

High performance trajectory tracking for multirotor Unmanned Aerial Vehicles (UAVs) is a fast growing research area due to the increase in popularity and demand. In many applications, the multirotor UAV dynamics would change in-flight resulting in performance degradation, or even instability, such that the control system is required to adapt its parameters to the new dynamics. In this paper, we developed a real-time identification approach based on Deep Neural Networks (DNNs) and the Modified Relay Feedback Test (MRFT) to optimally tune PID controllers suitable for aggressive trajectory tracking. We also propose a feedback linearization technique along with additional feedforward terms to achieve high trajectory tracking performance. In addition, we investigate and analyze different PID configurations for position controllers to maximize the tracking performance in the presence of wind disturbance and system parameter changes, and provide a systematic design methodology to trade-off performance for robustness. We prove the effectiveness and applicability of our developed approach through a set of experiments where accurate trajectory tracking is maintained despite significant changes to the UAV aerodynamic characteristics and the application of external wind. We demonstrate low discrepancy between simulation and experimental results which proves the potential of using the suggested approach for planning and fault detection tasks. The achieved tracking results on figure-eight trajectory is on par with the state-of-the-art.

1. Introduction

1.1. Motivation

Trajectory tracking problem for multirotor Unmanned Aerial Vehicles (UAVs) has attracted significant attention from the robotics research community in recent years. This is mainly due to the wide range of potential applications where accurate and precise trajectory tracking are needed. These applications include agriculture, entertainment, security, delivery, 3D Mapping etc. [33, 25]. For example, precision agriculture using multirotor UAVs require accurate spatio-temporal tracking to efficiently spray the pesticides at the place and the time it's needed [20]. Another example is the need for accurate trajectory tracking of the multirotors in entertainment applications to execute the required trajectory while avoiding any attainable collateral damage.

A new UAV application domain is enabled by the recent advancements in on-board UAV navigation [8, 21, 22]. When navigating cluttered environments, the UAV dynamically plans local trajectories. Following these trajectories in the presence of sensor uncertainty, external disturbances, and controller inaccuracies can be challenging. Moreover, some multirotor UAV applications would introduce system changes while in operation, for example installation of a specific payload to accomplish a certain task, such as a gripper or a camera [16, 34], or even package for delivery tasks. These payloads change the dynamics such as the mass, moment of inertia and aerodynamic behavior, which result in trajectory tracking performance degradation or even instability in certain cases. As a result, high performance trajectory tracking for multirotors attracted the attention of many researchers in recent years. Additional enhancement for the tracking performance would lead to improved operational safety, and minimization of losses and accidents in missions carried in tight or crowded areas. In this work, we address the problem of accurate aggressive trajectory tracking in the presence of external wind disturbance, and in the case of in-flight changes to the aerodynamic properties of the UAV.

Estimating multirotor aerodynamic effects is a challenging problem that is widely studied in literature [26, 15, 11, 9, 32]. Its complexity arises from the dependency on many system states; not only the nonlinear relation with the velocity, but also on the projected area (which depends on the attitude and velocity direction), induced drag due to the propulsion system and other complex phenomena [5, 26]. Furthermore, it is much harder to achieve the desired performance at high velocities and accelerations because of the increased aerodynamic effects that are difficult to model and compensate for due to their complexity. Thus, aerodynamics accurate modeling of a multirotor is a research challenge, and proper

*Corresponding authors, equally contributing.
Email addresses: 100052628@ku.ac.ae (AbdulAziz Y. AlKayas) ; mohamad.chehadeh@ku.ac.ae (Mohamad Chehadeh) ; abdulla.ayyad@ku.ac.ae (Abdulla Ayyad) ; yahya.zweiri@ku.ac.ae (Yahya Zweiri).
ORCID(s): 0000-0002-3218-724X (A.Y. AlKayas); 0000-0002-9430-3349 (M. Chehadeh); 0000-0002-3006-2320 (A. Ayyad); 0000-0003-4331-7254 (Y. Zweiri)

knowledge of such dynamics is essential to guarantee high performance.

1.2. Related Work

Trajectory tracking problem for UAVs is an active research topic in the robotics community. Various algorithms and system components work in harmony to complete a trajectory tracking task. Trajectory tracking problem can be mainly split into two parts: feasible trajectory generation, and closed loop error minimization controller (for simplicity and compatibility with literature, we refer to it as trajectory tracking in this work), where this work is mainly concerned with the latter. A trajectory reference needs to be generated prior to tracking and the most adopted class of techniques is to use piece-wise polynomial trajectories [19]. Tracking performance of such trajectories can be greatly enhanced when reference states are generated, which requires the generated trajectory to be continuous, and the system to be differentially flat. In some sense, generating reference states transforms a trajectory tracking problem into a state tracking problem, greatly enhancing the tracking performance as shown by the results reported in [19, 11, 30].

Trajectory tracking methods can be classified into two broad categories: feedforward and robust feedback methods. Feedforward methods rely on repeatable disturbance models to compensate for them through inversion. The pioneering work of [28] used iterative learning to synthesize a drag description and it is associated feedforward terms. A more recent work by [11] built up on the useful property of differential flatness where the authors proved that a multirotor model with linear rotor drag is differentially flat. The flatness property is utilized to compute feedforward control terms to achieve accurate tracking of trajectories which has efficiency advantages in implementation and tuning compared to iterative learning methods. The computation of each of these feedforward terms depends on the rotor drag coefficients which are obtained through an optimization method and are specific for every trajectory to be followed. The results showed enhanced performance in Lemniscate and circular trajectories reaching velocities up to 5 m/s and the authors manually compensated for time delays in the system. A more recent work from the same group could generalize over all trajectory shapes [31]. The authors used a Model Predictive Controller (MPC) for multirotors with the aerodynamic effects modeled using Gaussian processes (GPs). By training using previously recorded flight data, the GPs can predict the error in acceleration due to aerodynamic drag given the velocity of the multirotor. The controller was able to achieve 70% reduction in the tracking error for aggressive trajectories such as the Lemniscate of Gerono trajectory, reaching velocities up to 14 m/s and accelerations exceeding 4g. A drawback of this method is being computationally demanding such that a ground computer is required to perform MPC calculations. Another work by [29] leveraged a learning based technique to produce adequate feedforward terms to perform accurate trajectory tracking in the presence of modeling and disturbance uncertainties. In a similar way to the other feedforward tuning methodologies, a regression algorithm learned a drag model based on flight data. All these methods [28, 11, 31, 29] require extensive data collection and offline optimization to build up a drag or disturbance model, which limits the suitability for real-time adaptation. Also the optimized model can be biased towards the training data, and might under perform for unseen scenarios. For example, in [11], the drag model is refined for every considered trajectory shape. Trajectory tracking performance with feedforward methods can be significantly reduced due to the presence of external wind in the environment.

The other category of trajectory trackers utilize robust or adaptive controller structure and gains. One of the most common approaches for trajectory tracking is feedback linearization with differential flatness as suggested in [19]. The recent work in [30] suggested an incremental nonlinear dynamic inversion (INDI) approach and was able to achieve high-performance trajectory tracking control scheme capable of successfully doing aggressive maneuvers (high accelerations and velocities) without the need for accurate modeling or knowledge about the aerodynamic parameters of the multirotor. They utilized the differential flatness property of the multirotor to generate the trajectory reference derivatives (velocity, acceleration, jerk and snap). To compensate for the inaccuracies in the model as well as the external disturbance due to aerodynamic drag, INDI control technique was used and arranged in a setting that requires high rate measurements of motor rotational speeds, and full states measurements. This is a drawback as such measurements are not available with the majority of the multirotor UAVs hardware currently deployed. The recent work of [13] utilized acceleration error scheme instead of the common feedback linearization based approaches. This approach requires a clean, lag-free acceleration measurement which was obtained by designing a novel regression based filter that removes accelerometer noise caused by propeller rotations (the accelerometer measurement comes from the IMU). This has a clear advantage over [30] as no additional sensors are required. In [24], the authors used model learning approach that adapts controller gains and showed improvement in tracking accuracy in the presence of external wind with speeds reaching $6.2 m/s$. However the achieved tracking performance was incomparable with the tracking performance for the wind free case. The presented experiments in [24] were demonstrated in a scenario where the wind speed across all trajectory segments was constant. Other related work was based on combining different control and estimation methods to achieve the desired performance, like in [23] where the authors presented an adaptive fuzzy terminal sliding mode controller (AFTSMC) capable of tracking a predefined flight path under model uncertainty and external disturbances. Another work also based on the combination approach was investigated in [12] where a multiple observers based anti-disturbance control (MOBADC) scheme was developed to enhance the tracking performance under wind and suspended payloads disturbances. One of the drawbacks was the need for partial information about the payload to maximize the

rejection performance, but it showed good performance for the case of wind disturbance.

In all the surveyed work, there was no clear and systematic methodology for the automatic tuning of controller gains for trajectory tracking and adaptation to system changes; rather, it depended on the human expertise or the extensive experimental data to achieve a satisfactory tracking performance. Based on the surveyed literature, it is not possible with the current state-of-the-art to obtain knowledge about the aerodynamic parameters in a form that is suitable for real-time controller synthesis. Also, current data-driven approaches lack predictability of the system response to unseen operating environments. Clearly, the current literature lacks a systematic simple and safe identification and tuning methodology for accurate high speed trajectory tracking in the presence of external wind disturbances.

1.3. Contribution

In this paper, we propose a systematic approach for tuning and adapting controller parameters based on Deep Neural Networks and the Modified Relay Feedback Test (DNN-MRFT) for accurate trajectory tracking with disturbance attenuation capability. The proposed approach can adapt in real-time to changes in system dynamics that could happen during the mission, thus maintaining optimal trajectory tracking performance at all mission stages. DNN-MRFT ensures stability and sub-optimality performance bounds which we show to be negligible, thus optimality of performance can be claimed. DNN-MRFT runs in real-time on on-board computers and requires a few seconds to obtain optimal controller parameters for all UAV control loops.

We demonstrate the validity and efficiency of our approach by introducing significant change to the system dynamics during flight that would cause controller performance deterioration, which are four 12 cm wide and 40 cm long balloons fixed on each side of the multirotor. The new system is then identified and tuned using the DNN-MRFT approach regaining the state-of-the-art tracking performance for a Lemniscate of Gerono trajectory.

We also present the analysis of different tuning approaches for Proportional-Derivative (PD) and Proportional-Integral-Derivative (PID) controllers and their tracking performance under model parameter changes as well as external wind disturbances. The obtained results show a trajectory tracking performance that is on par with the state-of-the-art control methods, and shows unique capability for attenuating external disturbances where the RMSE of tracking was 3.59 cm. A video of the experiments can be found in [1].

1.4. Structure of the Paper

The paper is structured as follows. The model of multirotor UAVs is presented in Section 2. The suggested control structure is presented in 3. The methodology for identifying unknown system parameters, and the tuning of the controller parameters is presented in Section 4. Finally, simulation and experimental results are presented in Section 5.

2. Modeling Dynamics

In this section, we present a nonlinear model of the multirotor UAVs that accounts for the actuator dynamics and digital delays in the system. We then present a linearized version of the nonlinear model that is suitable for identification and controller tuning. We choose a quadrotor as our simulation and experimentation platform, however this approach is directly extendable to any other symmetric multirotor UAVs.

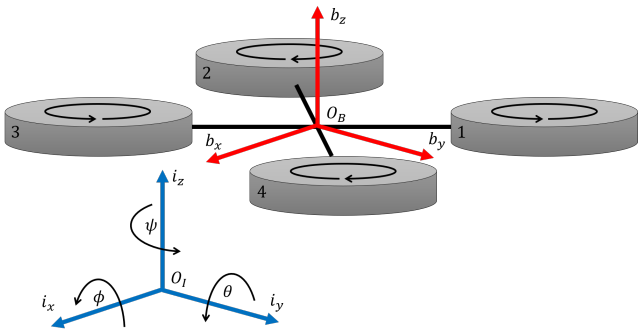

Figure 1: Schematic representation of the quadrotor and the coordinate systems used.

2.1. Reference Frames and Conventions

We define an Earth-fixed right-handed inertial frame $\mathcal{F}_I$ with the basis $\mathbf{i_z}$ pointing upwards opposite to gravity. For simplicity, we can express a basis or a vector with respect to a reference frame, e.g. the position vector ${}^I\mathbf{p} = [x\ y\ z]^T$ is expressed in the inertial frame. Rotations around the inertial axes are given by the Euler angles $\eta = [\phi\ \theta\ \psi]^T$ which describe the roll, pitch and yaw respectively. Similarly, we define the body-fixed reference frame $\mathcal{F}_B$ to have a basis $\mathbf{b_z}$ that is parallel to the thrust force produced by the actuators, and is centered at the UAV center of gravity (CoG). For convenience, we define the horizon frame $\mathcal{F}_H$ which has its origin coincident with the origin of $\mathcal{F}_I$. The reference frame $\mathcal{F}_H$ is yaw aligned with $\mathcal{F}_B$, while the pair $\{\boldsymbol{h_z}, \boldsymbol{i_z}\}$ is always coincident. The orientation of the multirotor can be described by the rotation matrix ${}^I_B R$ which is a transformation defined in the SO(3) Lie group where the identity of the group is defined as ${}^I_B R {}^B_I R = \mathbf{I}$. The Lie algebra $\mathfrak{so}(3)$ is defined around the identity element of the group with the rotational velocity vector $\boldsymbol{\omega} = [p\ q\ r]^T$ [14].

2.2. Nonlinear Multirotor Model

The thrust force and pitching or rolling torques exerted by each propeller are described by:

$$\begin{aligned} f_i &= k_f \Omega_i^2, \\ \tau_{\phi,\theta_i} &= k_f l_{\phi,\theta} \Omega_i^2. \end{aligned} \tag{1}$$

$$i \in \{1, ..., n_p\}$$

Where i here denotes the rotor index. For the case of a quadrotor, we have the number of rotors $n_p = 4$. The yawing torque is different in nature than the rolling and pitching torques as it is caused by the reactive torque from the motors and it can be described by the following equation:

$$\tau_{\psi_i} = (-1)^{i+1} k_\tau \Omega_i^2 \tag{2}$$

Thus, the actuators forces and torques can be summarized in a matrix equation relating them to the angular speed Ω of each propeller:

$$\begin{bmatrix} f_T \\ \tau_\phi \\ \tau_\theta \\ \tau_\psi \end{bmatrix} = \begin{bmatrix} k_f & k_f & k_f & k_f \\ k_f l_\phi & -k_f l_\phi & -k_f l_\phi & k_f l_\phi \\ k_f l_\theta & k_f l_\theta & -k_f l_\theta & -k_f l_\theta \\ k_\tau & -k_\tau & k_\tau & -k_\tau \end{bmatrix} \begin{bmatrix} \Omega_1^2 \\ \Omega_2^2 \\ \Omega_3^2 \\ \Omega_4^2 \end{bmatrix} \tag{3}$$

A multirotor is considered a rigid body in $\mathbb{R}^3$, having 6 degrees-of-freedom (DOF) and subject to forces and torques in $\mathbb{R}^3$. It is assumed that the weight of the multirotor is acting on CoG which is coincident with the body frame ${}^B\mathcal{F}$ origin, and assumed to be symmetric around all axes. Thus, the inertia matrix is $\boldsymbol{J} = diag(J_x, J_y, J_z)$. The governing equations for such bodies can be described by Newton-Euler equations described in the body frame as follows:

$$\begin{bmatrix} m\mathbf{I}_{3\times3} & 0_{3\times3} \\ 0_{3\times3} & \boldsymbol{J} \end{bmatrix} \begin{bmatrix} \dot{\boldsymbol{V}} \\ \dot{\boldsymbol{\omega}} \end{bmatrix} = \begin{bmatrix} {}^B\boldsymbol{F} \\ {}^B\boldsymbol{\tau} \end{bmatrix} \tag{4}$$

$${}^B\boldsymbol{F} = f_T \boldsymbol{b_z} - {}^B_I R m g \boldsymbol{i_z} - \boldsymbol{\alpha} \tag{5}$$

$${}^B\boldsymbol{\tau} = \begin{bmatrix} \tau_\phi \\ \tau_\theta \\ \tau_\psi \end{bmatrix} - \boldsymbol{\lambda} \tag{6}$$

where $\dot{\boldsymbol{p}} = {}^I_B R \boldsymbol{V}$, m is the mass, and $\boldsymbol{\alpha}$ and $\boldsymbol{\lambda}$ are arbitrary functions that describe the translational and rotational drag forces acting on the multirotors body respectively.

From equations (4),(5) and (6) and neglecting the cross-coupling dynamics due to their small and mitigated effect due to the closed loop performance, we achieve a simplified multirotor model:

$$\begin{aligned}
{}^I\ddot{p}_x &= \frac{1}{m}\left((c_\psi s_\theta c_\phi + s_\psi s_\phi) f_T - \alpha_x({}^I\dot{p}_x, \eta, \Omega)\right), \\
{}^I\ddot{p}_y &= \frac{1}{m}\left((s_\psi s_\theta c_\phi - c_\psi s_\phi) f_T - \alpha_y({}^I\dot{p}_y, \eta, \Omega)\right), \\
{}^I\ddot{p}_z &= \frac{1}{m}\left(c_\phi c_\theta f_T - g - \alpha_z({}^I\dot{p}_z, \eta, \Omega)\right), \\
\ddot{\phi} &= \frac{1}{J_x}\left(\tau_\phi - \lambda_\phi(\omega, \Omega)\right), \\
\ddot{\theta} &= \frac{1}{J_y}\left(\tau_\theta - \lambda_\theta(\omega, \Omega)\right), \\
\ddot{\psi} &= \frac{1}{J_z}\left(\tau_\psi - \lambda_\psi(\omega, \Omega)\right).
\end{aligned} \tag{7}$$

2.3. Actuator Dynamics

Brushless Direct Current (BLDC) motors is the common choice as an actuator for multirotors, and each motor requires a dedicated electronic speed controller (ESC). The ESC receives a thrust reference u_i and produces a thrust force f_i. This relationship can be approximated well by a First Order Plus Time Delay (FOPTD) transfer function as investigated in [10, 9]:

$$G_{prop}(s) = \frac{K_{eq} e^{-\tau_{act} s}}{T_{prop} s + 1} \tag{8}$$

Usually time delay is omitted from the models widely adopted in literature [19, 11]. From our experimentation and numerical simulations, we could not achieve acceptable tuning results when time delay is omitted [9, 3]. Other researchers could minimize the effect of the omission of time delay by using high throughput sensor measurements, and full state system measurements by using additional sensors. Our approach alleviates such measurement requirements, thus it generalizes for almost all multirotor UAV hardware that exist in the market.

2.4. Linearized Attitude and Altitude Dynamics

Both the attitude and altitude dynamics can be approximated by a first order system plus integrator [26] which includes a linear drag term. This model showed good accuracy and performance when used with the DNN-MRFT approach in [3]. So these dynamics can be described by the following transfer function:

$$G_{att,alt}(s) = \frac{K_{eq}}{s(T_1 s + 1)} \tag{9}$$

By cascading both transfer functions in (9) and (8) we acquire a second order system plus integrator plus time delay (SOIPTD) to represent the inner loop dynamics of a multirotor (i.e. attitude and altitude dynamics):

$$G_{inner}(s) = \frac{K_{eq} e^{-\tau_{in} s}}{s(T_{prop} s + 1)(T_1 s + 1)} \tag{10}$$

A more detailed representation of the inner loop dynamics with a PD feedback controller can be shown in Figure 2. Because drag is included in the model, the tuning process will suggest optimal parameters that take it into account without requiring model inversion for drag cancellation. The suggested lumped parameter system representation for identification and tuning of controllers refrain us from requiring a prior knowledge for any of the physical parameters showed earlier in the nonlinear model which is convenient in practice.

2.5. Linearized Side Motion Dynamics

As an underactuated system, the multirotor cannot achieve side (horizontal) motion through direct actuation commands,

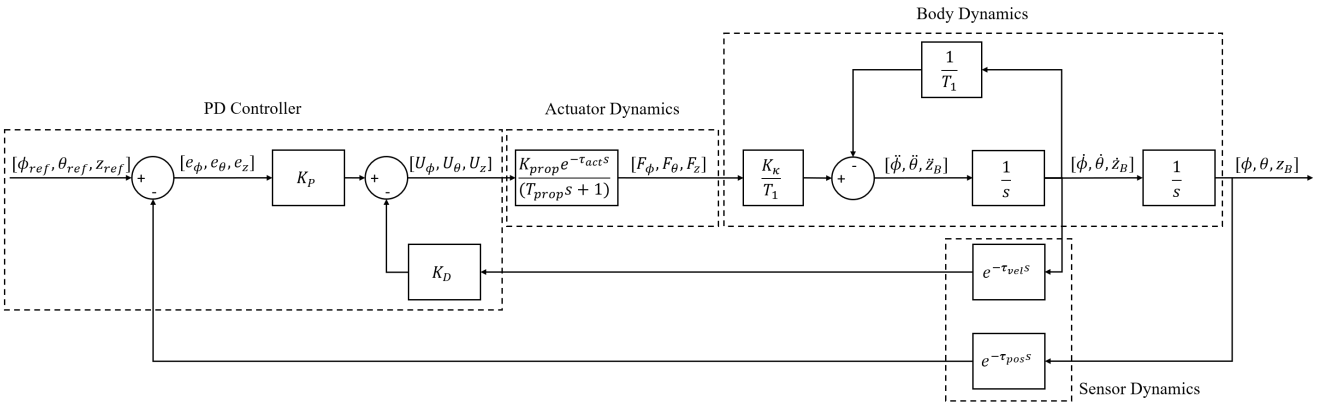

Figure 2: Generalized model used for attitude and altitude (ϕ, θ, z_B) dynamics with PD feedback controller.

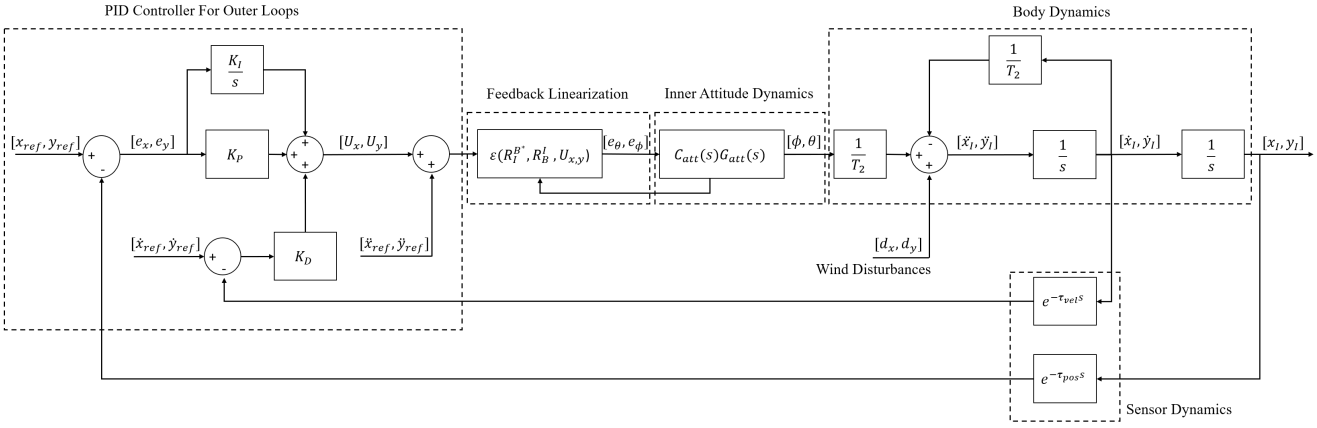

Figure 3: Generalized model used for horizontal motion (x_I, y_I) dynamics with PID feedback controller.

but instead it is achieved through the attitude of the multirotor. A simplified model for such dynamics was investigated in [4]:

$$G_{outer}(s) = \frac{X(s)}{\phi(s)} = \frac{K_{eq}e^{-\tau_{out}s}}{s(T_2 s + 1)} \tag{11}$$

We can combine equations (10) and (11) to acquire the side motion dynamics described by:

$$G_{side}(s) = \frac{K_{eq}e^{-(\tau_{in}+\tau_{out})s}}{s^2(T_{prop}s+1)(T_1 s+1)(T_2 s+1)}, \tag{12}$$

a more detailed representation of the dynamics with a PID controller is presented in Figure 3. Drag is assumed to be linear and overall, we have now two sets of rotational and translational drag terms modelled by the time constants T_1 and T_2 respectively.

3. Controller Design

We incorporate different techniques of control such as PID controllers, feedback linearization and feedforward terms. These techniques are incorporated to maximize the tracking performance of the multirotor. In this work, we are only using a PD controller for the attitude control of the multirotor. As for the position controller, we used different controllers tuned using different methods that will be discussed in section 3.4. It is also worth pointing out the use of the estimated velocity of the multirotor instead of differentiation of the error as shown in Figures 2,3, to avoid derivative kick. A kinematic based Kalman filter is used to provide smooth velocity and position estimates at the IMU update rate.

3.1. Feedback Linearization

We use a feedback linearization approach similar to the approaches suggested in [19, 11]. The position controllers provide the control output acceleration vector ${}^I\boldsymbol{a}^c$ as follows:

$$\begin{aligned} {}^I\boldsymbol{a}^c = {}^I_H R\big(\boldsymbol{K}_P \odot {}^H({}^I\boldsymbol{p}^{ref} - {}^I\boldsymbol{p}) + \boldsymbol{K}_D \odot {}^H({}^I\dot{\boldsymbol{p}}^{ref} - {}^I\dot{\boldsymbol{p}}) \\ + \boldsymbol{K}_I \odot {}^H({}^I\bar{\boldsymbol{e}}_{\boldsymbol{p}})\big) + {}^I\boldsymbol{a}^{ref} \end{aligned} \tag{13}$$

where $\odot$ is the Hadamard product, $\bar{e}_p$ is an augmented state due to the integration of the error in position, and reference position and its derivatives are denoted by the ref superscript. The vectors $\boldsymbol{K}_P$, $\boldsymbol{K}_D$, and $\boldsymbol{K}_I$ are fixed controller

gains. At this stage, it is convenient to write Equation (5) in a mass normalized form in the inertial frame:

$$^{I}\boldsymbol{a} = {}^{I}_{B}R a_T \boldsymbol{b_z} - g\boldsymbol{i_z} \tag{14}$$

But a_T isn't a measured quantity in our system so it is assumed to be the same as the commanded mass normalized thrust a_T^* (defined in Equation (20). Note that this simplification assumes no actuator dynamics. This is a valid assumption as long as the frequency components of the followed trajectories are much smaller than the frequency bandwidth of the actuator dynamics. Also, g is not observable but what is important is to find the acceleration command a_g that compensates for it. In our case, we estimate a_g during hover, or alternatively it can be found using bench experiments. Lastly, drag dynamics are dropped from Equation (14) which is a simplification to the feedforward terms fed to the motors. These drag dynamics are accounted for in the identification algorithm, and hence they are accounted for in the feedback controller gains.

The desired acceleration output, $^{I}\boldsymbol{a}^*$, that is used to calculate motor commands and attitude loops references is given by:

$$^{I}\boldsymbol{a}^* = {}^{I}\boldsymbol{a}^c + a_g\boldsymbol{i_z} \tag{15}$$

For convenience, we then define a temporal reference frame $^{B^*}\mathcal{F}$ that represents the desired attitude with the basis $\mathbf{b}_\mathbf{z}^*$ aligned with $^{I}\boldsymbol{a}^*$ as follows:

$$^{I}\boldsymbol{b}_z^*(+) = \frac{^{I}\boldsymbol{a}^*}{\|^{I}\boldsymbol{a}^*\|} \tag{16}$$

$$^{I}\boldsymbol{b}_y^*(+) = \frac{^{I}\boldsymbol{b}_z^* \times [\cos(\psi_{ref})\ \ \sin(\psi_{ref})\ 0]^T}{\|^{I}\boldsymbol{b}_z^* \times [\cos(\psi_{ref})\ \ \sin(\psi_{ref})\ 0]^T\|} \tag{17}$$

$$^{I}\boldsymbol{b}_x^*(+) = {}^{I}\boldsymbol{b}_y^* \times {}^{I}\boldsymbol{b}_z^* \tag{18}$$

Therefore the roll, pitch and yaw components of the orientation errors can be computed as follows:

$$\begin{bmatrix} e_\phi \\ e_\theta \\ e_\psi \end{bmatrix} = \boldsymbol{\varepsilon}({}^{B^*}_{I}R\, {}^{I}_{B}R) \tag{19}$$

where $\boldsymbol{\varepsilon}$ is a function that converts the rotation matrix into the corresponding rotation vector representation of the attitude based on the inverse of the Rodrigues' rotation formula. Finally, we can calculate the collective thrust command u_z as:

$$u_z = k_b\, {}^{I}\boldsymbol{a}^* \cdot {}^{I}\boldsymbol{b_z} \tag{20}$$

where k_b is a dimensionless constant that maps the commanded acceleration to ESC command.

3.2. Trajectory Generation

In our work we choose Lemniscate of Gerono (also known as the figure-eight curve) trajectory with fixed altitude as our testing and benchmarking trajectory. It can be described by the following equations:

$$p_y^{ref}(t) = r\cos(\sigma(t)) \tag{21}$$

$$p_x^{ref}(t) = \frac{r\sin(2\sigma(t))}{2} \tag{22}$$

$$\sigma(t) = \sum_{i=0}^{n} b_i t^i \tag{23}$$

Where $\sigma(t)$ is a polynomial of n^{th} order, b_i is a polynomial coefficient, and r is the trajectory radius. We follow the work of [19] in optimizing $\sigma(t)$ in order to minimize the integral of the square of a chosen trajectory derivative over its period while enforcing a set of initial and terminal constraints. We have used the derivative of the generated trajectory, $\dot{p}_x^{ref}$ and $\dot{p}_y^{ref}$ as shown in Equation (13) to enhance the tracking performance. We also used the second derivative $\ddot{p}_x^{ref}$ and $\ddot{p}_y^{ref}$ as an additional feedforward input to $^{I}\boldsymbol{a}^c$ as shown in Equation (13). Higher derivatives beyond the second were not included in the control for a couple of reasons, although it would enhance the tracking performance, we needed knowledge about the generated thrust rate and the angular speed of the propeller which are unavailable.

The overall linearized and decoupled closed-loop system dynamics including the feedforward reference signals provided by the trajectory generator is given by:

$$\frac{X(s)}{R(s)} = \frac{G_{inner,cl}G_{outer}(C_{outer} + s^2)}{1 + G_{inner,cl}G_{outer}C_{outer}} \tag{24}$$

where $G_{inner,cl}$ is the closed loop inner dynamics (i.e. with inner loop controller), and C_{outer} is the outer loop feedback controller. The $G_{inner,cl}G_{outer}s^2$ term in the numerator, which is due to the use of the feedforward reference signal, reduces the relative degree of the system. Such reduction in the relative degree of the system results in a faster system response.

3.3. Controller Structure Selection

We could use either PID or PD control structure for the outer or the inner control loops. The selection depends on a few factors, and a single control structure cannot be the best for all scenarios (e.g. external disturbance, reference signal type, robustness, etc.). A PD controller applied to the inner attitude loops resulted in a lower rising time T_r compared to the PID but would result in a steady state error due to CoG or motor thrusts imbalance. The outer loop controller can compensate for such steady state errors in the inner loops. Steady state analysis is therefore limited to the case when a PD controller is used in the inner loops, and a PD or a PID

Controller Configuration	e_{ss} due to reference		e_{ss} due to disturbance	
	Step	Ramp	Step	Ramp
PD inner PD outer	0	$\frac{1}{1+K_{P_o}K_o}$	$-\frac{K_o}{1+K_{P_o}K_o}$	$-\infty$
PD inner PID outer	0	0	0	$-\frac{1}{K_{I_o}}$

Table 1
Steady state errors for different inputs references and disturbances.

controller is used in the outer loops. For this analysis the system structure given in the Figures 2,3 will be used with the following simplifications:

- Feedback linearization will be ignored, obviously due to linearization around nominal operating point.
- Velocity and acceleration reference inputs are set to zeros.

The results of the analysis are summarized in Table (1). It can be seen that the PD inner PID outer configuration is a suitable choice for error minimization for both varying references and constant disturbances. Tuning for the PID controller configuration will be based on ramp input reference. We will also consider the PD inner PD outer configuration tuned for step input based on its high performance and consistency seen in practice. The PD inner PD outer configuration suffers steady-state errors except for a step reference input, but its performance can be improved by using the higher order references as discussed in section 3.2.

3.4. Controller Tuning

The tuning is mainly based on minimizing a cost function Q, which is a function of the error to a specific input to the system. In our work we will choose Q the ISE performance index realized by:

$$Q_{ISE} = \int_0^\infty (x^{ref}(t) - x(t))^2 dt \tag{25}$$

Other performance indices were investigated, such as IAE, ITAE and ITSE. Settling on the ISE over the others was based on the speed of the response, where we found that controllers tuned based on the ISE provided the quickest response. The tuning is conducted using MATLAB and Simulink. The error is calculated based on the system structure shown in Figures 2,3. We used the derivative free Nelder-Mead simplex algorithm which is realized by the *"fminsearch"* optimization function [18]. The objective of the optimization function is to minimize the error function and the decision variables are the controller parameters. We found that the optimizer usually get stuck at local minimas when tuning PID controller parameters in the form presented in Equation ((13)). We found that parameterizing the control parameters using the *homogeneous tuning rules* avoided the local minima issue, and resulted in a much faster optimization time. The homogeneous tuning rules are given by [6]:

$$K_c = c_1 \frac{4h}{\pi a_0} \ , \ T_I = c_2 \frac{2\pi}{\Omega_0} \ , \ T_D = c_3 \frac{2\pi}{\Omega_0} \tag{26}$$

Here c_1, c_2, c_3 are constant parameters which define the homogeneous tuning rule. Such parameterization greatly simplifies the representation of the closed loop system as it would be provided in a form that is invariant to time and static gain scaling. The homogeneous tuning rule is related to the gain and phase margins of the system by two sets of equations [7]. These equations govern a relation between the homogeneous tuning rule parameters and allow us to exploit the time and gain invariance properties of the tuning rule. The phase margin constrain equations are given by:

$$\begin{aligned} \beta &= \sin\left(\varphi_m + arctan\left(\frac{1}{2\pi c_2} - 2\pi c_3\right)\right), \\ c_1 &\sqrt{1 + \left(2\pi c_3 - \frac{1}{2\pi c_2}\right)^2} = 1, \end{aligned} \tag{27}$$

where φ_m is the phase margin of the closed loop system. Since we are tuning only a PD controller in the first method, then c_2, the constant corresponding to the integral term, will be equal to zero.

On the other hand, the gain margin constrain equations are given by:

$$\begin{aligned} \beta &= -\frac{2\pi c_3 - \frac{1}{2\pi c_2}}{\sqrt{1 + \left(2\pi c_3 - \frac{1}{2\pi c_2}\right)^2}}, \\ \gamma_m c_1 &\sqrt{1 + \left(2\pi c_3 - \frac{1}{2\pi c_2}\right)^2} = 1. \end{aligned} \tag{28}$$

where γ_m is the gain margin of the closed loop system. By utilizing the Equations (27) and (28), we can have the freedom in the selection of the decision variables for optimization. For example, in a phase margin based tuning, we can optimize based on φ_m, c_1, and c_3 and calculate the other parameters directly. Because φ_m is a decision variable, we can impose minimum and maximum phase margins of the system which is very useful for robust tuning. The same applies for the gain margin tuning.

4. Identification with DNN-MRFT

In this section, we will discuss the different approaches used in the tuning of our controller and how does it fit with the DNN-MRFT approach [3, 4]. DNN-MRFT performs identification in real-time within seconds and guarantees near

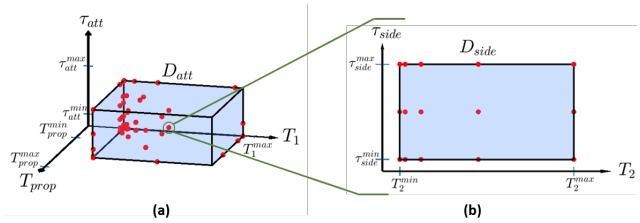

Figure 4: Illustration of discretized processes in the parameter space. (a) D_{att} and D_{alt} domains are discretized to obtain processes of $\bar{D}_{att}$ and $\bar{D}_{alt}$ shown by the red dots. (b) For each member process of $\bar{D}_{att}$, a different set of $\bar{D}_{side}$ processes are obtained.

optimal performance. These features were demonstrated by the experiments in [4], where UAVs of different sizes were able to perform full identification from take-off.

4.1. Generating Periodic Motion

The idea of the identification is to excite a periodic motion in the system that reveals the unknown system dynamics. Measured system output is then fed to a deep neural network (DNN) which classifies the unknown process parameters and provides near optimal tuning. The periodic motion is excited using the modified relay feedback test (MRFT) which is given by [7]:

$$u_M(t) = \begin{cases} h & : e(t) \geq b_1 \ \vee \ (e(t) > -b_2 \ \wedge \ u_M(t-) = h) \\ -h & : e(t) \leq -b_2 \ \vee \ (e(t) < b_1 \ \wedge \ u_M(t-) = -h) \end{cases} \quad (29)$$

where $b_1 = -\beta e_{min}$ and $b_2 = \beta e_{max}$. $e_{max} > 0$ and $e_{min} < 0$ are respectively the last maximum and minimum values of the error signal after crossing the zero level; and $u_M(t-) = lim_{\epsilon \to 0^+} u_M(t-\epsilon)$ is the last control output. Initially the maximum and minimum error values are set as: $e_{max} = e_{min} = 0$. β is a tunable parameter that defines the phase of the excited oscillations. Based on the describing function (DF) method, it could be shown that the MRFT achieves oscillations at the phase angle defined by the parameter β by satisfying the HB equation [2]:

$$N_d(a_0)G(j\Omega_0) = -1 \quad (30)$$

The DF of MRFT is presented in [7] as:

$$N_d(a_0) = \frac{4h}{\pi a_0}(\sqrt{1-\beta^2} - j\beta) \quad (31)$$

Stability of the periodic motion for the considered multirotor UAV dynamics is discussed in [4].

4.2. Identification Steps

DNN-MRFT handles identification as a classification problem. Process classes in the unknown process parameters' space are sampled based on the relative sensitivity metric and the minmax approach [27]. The relative sensitivity function indicates the robustness of the system to the changes in process parameters and is governed by the following equation:

$$J_{ij} = \frac{Q(C_i, G_j) - Q(C_j, G_j)}{Q(C_j, G_j)} \times 100\% \quad (32)$$

where J_{ij} represents the degradation in performance due to applying controller C_i, which is the optimal controller for the process G_i and a sub-optimal controller for the process G_j. Q denotes the integral square error (ISE) of the step response of the closed loop system. Note that $J_{ij} \neq J_{ji}$ so we define $J_{(ij)} = max(J_{ij}, J_{ji})$.

We summarize the identification steps reported in [3, 4] for the identification of the inner loop and outer loop dynamics as follows:

1. Identify the domain of the unknown time parameters T_{prop}, T_1, T_2, τ_{in}, and τ_{out}. We select these ranges based on prominent multirotor UAV sizes and designs (we include multirotor UAVs that span few centimeters to a few meters). Namely the selected parameters ranges are the same for those in [4] and they are $T_{prop} \in [0.015, 0.3]$, $T_1 \in [0.2, 2]$, $T_2 \in [0.2, 6]$, $\tau_{in} \in [0.0005, 0.03]$, and $\tau_{out} \in [0.0005, 0.15]$. Altitude parameters domain D_{alt}, attitude parameters domain D_{att}, and side motion parameters domain D_{side} are formed based on the selected parameters' domains.
2. Relative sensitivity value is selected to be $J^* = J_{(ij)} = 10\%$ which means that adjacent discretized processes would provide at worst 10% drop in closed loop system performance.
3. Discretize D_{att} and D_{alt} as illustrated in Fig. 4 (a) and outlined in [3] based on J^* value to obtain discretized domains $\bar{D}_{att}$ and $\bar{D}_{alt}$.
4. Discretize the outer loop domain D_{side} for every discretized inner loop process in $\bar{D}_{att}$ as shown in Fig. 4 (b). This will result in a set of discretized domains $\{\bar{D}_{side,1}, ..., \bar{D}_{side,n}\}$ where n is the number of processes in $\bar{D}_{att}$ [4].
5. In simulation, generate system responses for every process in $\bar{D}_{att}$ and $\bar{D}_{alt}$ based on $\beta = -0.73$ value reported in [3] and for $\bar{D}_{side,i}$ use β value that is specific for every process in $\bar{D}_{att}$.
6. Find the optimal controller for every discretized process in $\bar{D}_{att}$, $\bar{D}_{alt}$, and $\bar{D}_{side}$ using the tuning methodology presented in Section 3.4.
7. Train the DNN based on simulation data. Generated data is augmented with noise and process bias for better generalization. The output layer uses the modified softmax cost function derived in [3].
8. Finally, excite a periodic motion experimentally using MRFT algorithm shown in Equation (29) and feed the measured process output to the DNN for identification and obtaining controller parameters.

5. Results

In this section, we will show a set of trajectory tracking experiments with different controller tuning settings. First,

we present the adaptation capability to system dynamics changes, then we show the robust tuning effect and the behaviour when the system is subjected to system dynamics changes or external disturbances.

5.1. Experimental Setup

The quadrotor platform used in the experiments of this paper is the QUANSER QDrone. It has a carbon fiber frame with a protected propulsion system design that consists of four Cobra CM-2205/2100kv BLDCs and 6045 polycarbonate propellers. The QDrone weighs 1125 g with a thrust-to-weight ratio of 1.9. QDrone features Intel Aero Compute on-board embedded computer with the ability to be programmed through MATLAB/Simulink. The Madgwick filter [17] is used to estimate the attitude of the multirotor through the on-board BMI160 IMU Sensor. OptiTrack motion capture system was used to provide position and yaw measurements to the multirotor at 250 Hz.

In our flight experiments, we use Lemniscate of Gerono trajectory with dimensions of $3 \times 1.5m$ which is generated as described in Section 3.2, without imposing any actuator limits. The fastest trajectory we were able to achieve before reaching motors' upper limits took eight seconds to perform. In all flight experiments, we will compare the results with a nonlinear simulation model utilizing the parameters acquired from the DNN-MRFT identification.

To assess the trajectory tracking performance, we use two metrics, the first one is the root mean squared error (RMSE) which indicates how good the temporal tracking is:

$$RMSE = \sqrt{\frac{\sum_{i=1}^{N}(x - x^{ref})_i^2 + (y - y^{ref})_i^2}{N}} \tag{33}$$

where N is the number of the sampled data points in the trajectory. The second metric is the contouring error, which captures how good the spatial tracking is, and is defined by the minimum Euclidean distance between a given position measurement and the nearest point on the reference trajectory:

$$CE_i = \min\left(\sqrt{(x_i - x^{ref})^2 + (y_i - y^{ref})^2}\right) \tag{34}$$

It follows that we define the average of all summed contouring errors to be CE_{avg}, and the maximum contouring error to be $CE_{max} = \text{argmax}\, CE_i$.

5.2. Online Adaptation Capability

For this experiment, we use the PD inner PD outer controller structure. We found from simulations that using PD instead of PID for the outer loops resulted in the best tracking results. We also found that with the PID controller, we can impose high gain margins with slight drop in performance. High gain margin values ensure robustness against external wind disturbances and changes in platform aerodynamics. For these reasons, we chose to experimentally demonstrate online adaptation capability with PD controllers in the outer loop.

Figure 5: The QDrone with the dynamics changing payload installed.

The PD gains were tuned without imposing any robustness margins (i.e. phase margin or gain margin constraints). These gains were tuned based on DNN-MRFT identified system parameters. Three trajectory tracking flights were done in sequence. In the first flight, we used the PD controller tuned based on DNN-MRFT applied to the multirotor UAV without any payload attached (we refer to it as the base controller). The achieved tracking errors were as low as 2.6 cm which sets the new state-of-the-art in trajectory tracking performance for multirotor UAVs in the given range of velocities and platform sizes. We can compare this performance with the recent work of [11], where an error of 3.3 cm was achieved, approximated from a $4 \times 2m$ figure-eight trajectory with a similar maximum speed of around 3.2 m/s using a platform that has a thrust-to-weight ratio of 4. This shows that our performance is on par with the state-of-the-art, despite the platform limitations. Before the second flight and while the multirotor UAV is still in hover, we attach a payload to it to alter its aerodynamic properties. The lightweight payload consists of four 12 cm wide by 40 cm long balloons installed on each side of the UAV as shown in figure 5. While performing the second flight with the base controller, the platform exhibited instability and it crashed, apparently due to the altered dynamics. Before the third flight, we re-run DNN-MRFT identification and tuning; which is performed online and takes just a few seconds to adapt for the newly added payload. The achieved trajectory tracking error with the adapted controller on the platform with added payload is $3.42cm$, which is just slightly higher than the reported errors for the first flight. Table 3 summarizes the performance results for the online adaptation experiments. Also, Table 2 shows DNN-MRFT identification results for both the payload and the no payload cases. We can notice that the increase in the system overall gain which evidently resulted in the instability of Flight 2. These experiments scenario is shown in the video in [1]. The experimental and simulation results can be seen in Figure 6. Note the close match between the simulation and experimentation results. It is also worth noting that the identified parameters for the base system were used in the simulations. This match be-

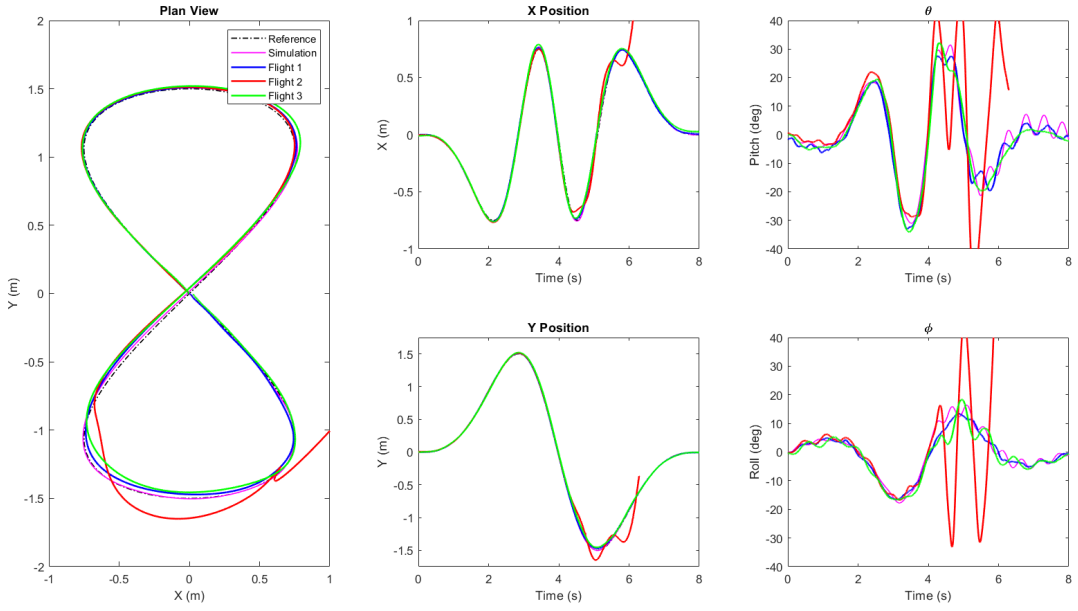

Figure 6: Tracking performance of the three flights with PD as outer loop controller:
Flight 1 (blue): Base Controller - Without Payload.
Flight 2 (red): Base Controller - With Payload. QDrone crashed resulting in discontinuation of data streaming.
Flight 3 (green): Adapted Controller - With Payload.

	K_{in}	K_{out}	T_{prop}	T_1	T_2	τ_{in}	τ_{out}
Without Payload	68	1.1516	0.064	0.2494	1.1629	0.0009	0.0005
With Payload	37.46	5.01	0.0498	0.1938	6	0.014	0.0005

Table 2
DNN-MRFT identification results for the QDrone with and without the payload.

	$RMSE(cm)$	$CE_{avg}(cm)$	$CE_{max}(cm)$
Flight 1	2.6	1.07	3.88
Flight 2	Unstable	Unstable	Unstable
Flight 3	3.42	1.76	8.01

Table 3
Performance results for the online adaptation experiments.
Flight 1: Base Controller - Without Payload.
Flight 2: Base Controller - With Payload.
Flight 3: Adapted Controller - With Payload.

tween simulation and experimentation provides a major advantage over other methods suggested in literature for trajectory tracking, as such accurate simulations can be used for efficient and safe flight planning.

The instability that occurred in the second flight where the base controller was used can be explained by simulating the identification results. Applying the base controller to the identified multirotor UAV process with payload resulted in a phase margin of $\varphi_m = 3.45^o$ and a gain margin of $\gamma_m = 1.12$. With such small stability margins it is likely that the nonlinearities in the system would alter the dynamics in a way that would result in instability, which was the case. On the other hand, the stability margins in the first and third flight scenarios were around $\varphi_m = 10^o$, $\gamma_m = 1.3$.

5.3. Tuning for Robust Tracking and Wind Disturbance Attenuation

This section demonstrates the performance of the second selected controller structure, PD for inner loops and PID for the outer loops. The outer loop PIDs are tuned for ramp reference with constraints on the gain margin for increased robustness. Figure 9 shows the performance versus robustness curve. Without imposing any gain margin constraints, the optimal ISE cost function evaluates to 0.0086 with a gain margin of $\gamma_m = 1.0574$. However, we chose to have a system with gain margin of $\gamma_m = 1.5$ and a increased ISE cost by 41.9% compared to the optimal for the sake of increased robustness.

Similar to the PD controller case, we have done two consecutive flight tests with the robust PID tuning: the first without payload, and the second with the payload installed. The performance was not noticeably altered due to the installation of the payload, on the contrary, the performance got better due to the increase in the systems gain as seen in the DNN-MRFT identification results in Table 2, thus sacrific-

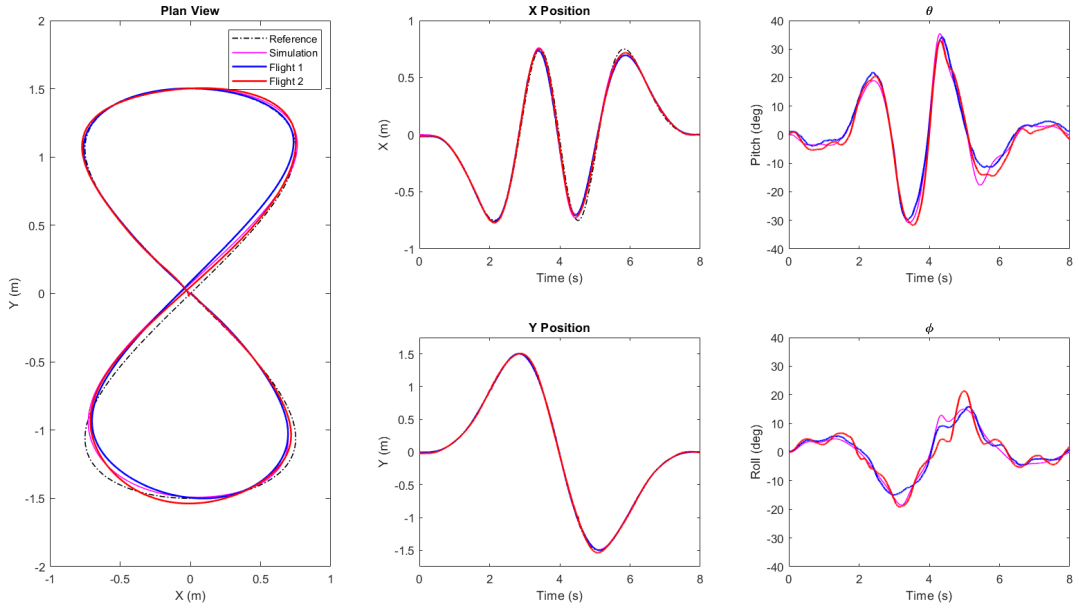

Figure 7: Tracking performance of the two PID scenarios (robust tuning).
Flight 1 (blue): Base Controller - Without Payload.
Flight 2 (red): Base Controller - With Payload.

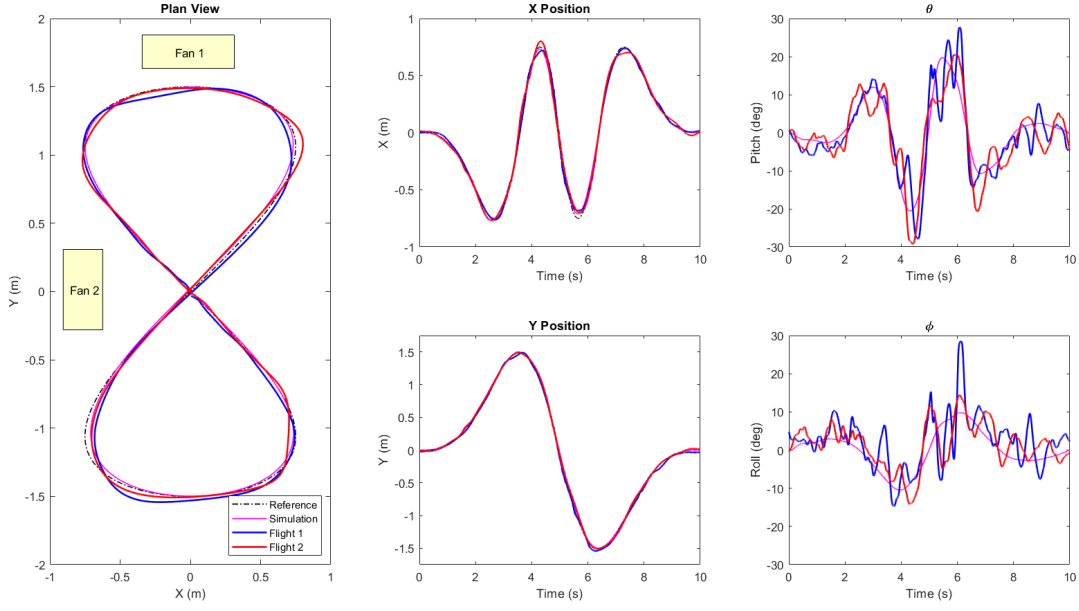

Figure 8: Tracking performance under wind disturbance. Fans locations indicated by the yellow boxes.
Flight 1 (blue): PD under wind disturbance.
Flight 2 (red): PID under wind disturbance.

ing some of the gain margin that the controller was tuned on. Results for the two flights can be seen in Figure 7 and Table 4.

Finally, we fly the same trajectory without the payload for ten seconds under high speed wind reaching $5m/s$ from the x and y directions with the robustly tuned PID gains. We could not fly the trajectory with a lap speed of eight seconds as the motors reached saturation when counteracting wind effect. We exploit the natural disturbance rejection capabilities that the system inherits from using the integral term and

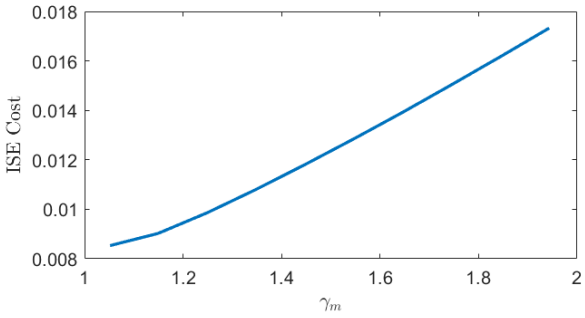

Figure 9: Performance robustness trade-off curve for PID controller with gain margin constraint.

	$RMSE(cm)$	$CE_{avg}(cm)$	$CE_{max}(cm)$
Flight 1	4.22	1.81	10.4
Flight 2	3.33	1.53	7.64

Table 4
Performance results for the robust tuning experiments.
Flight 1: Base Controller - Without Payload.
Flight 2: Base Controller - With Payload.

	$RMSE(cm)$	$CE_{avg}(cm)$	$CE_{max}(cm)$
Flight 1	3.78	1.99	7.33
Flight 2	3.59	1.47	5.26

Table 5
Performance results for the wind disturbance experiments.
Flight 1: PD under wind disturbance.
Flight 2: PID under wind disturbance.

test the performance under irregular high speed wind conditions. The tracking performance under wind conditions seen in Figure 8 is comparable with the wind-free case, disturbances was not included in simulations in the same figure. Table 5 summarizes the performance results for the wind disturbance experiments.

6. Conclusion

A controller tuning approach based on DNN-MRFT identification to perform accurate trajectory tracking was presented. The suggested approach provides several demonstrated advantages over existing methods in literature. First, controller parameters' tuning can be done systematically based on the real-time identification results of DNN-MRFT. This capability was demonstrated experimentally where the multirotor UAV was able to adapt to significant changes in the payload in-flight. The second advantage is the systematic ability to trade-off performance and robustness, which was demonstrated by the tuning of a robust PID controller that performed well despite payload changes and external wind. The third demonstrated advantage is the match between simulation and experimentation which can be used to realize efficient planning algorithms, fault detection, etc. The tuned multirotor UAV achieved state-of-the-art performance in tracking a Lemniscate of Gerono trajectory.

In future work, we aim to utilize high fidelity simulations to design real-time planning algorithms. A potential continuation of this work is to design a gain scheduling mechanism for improved control performance based on changing flight conditions. We have also observed some interesting limit cycle behaviour when using MRFT with feedback linearization. These limit cycles worth further investigations as they could be utilized for better identification of fast actuator and sensor dynamics.

Declaration of competing interest

The authors declare that they have no known competing financial interests or personal relationships that could have appeared to influence the work reported in this paper.

Acknowledgment

This work was supported by Khalifa University Grants CIRA-2020-082 and RC1-2018-KUCARS. We would like to thank Quanser team for their generous and timely support. We also thank Prof. Igor Boiko for the fruitful technical discussions. We also thank Eng. Mohammad Wahbah and Eng. Oussama Abdul Hay for helping in the preparation of the experimental setup.

References

[1] AlKayas, A.Y., Chehadeh, M., Ayyad, A., Zweiri, Y., 2021. Real-time Identification and Tuning of Multirotors using DNNs for Accurate Trajectory Tracking. URL: https://youtu.be/CdnW0Slhi34.

[2] Atherton, D., 1975. Nonlinear Control Engineering: Describing Function Analysis and Design. Van Nostrand Reinhold, London.

[3] Ayyad, A., Chehadeh, M., Awad, M.I., Zweiri, Y., 2020. Real-time system identification using deep learning for linear processes with application to unmanned aerial vehicles. IEEE Access 8, 122539–122553.

[4] Ayyad, A., Silva, P., Chehadeh, M., Wahbah, M., Hay, O.A., Boiko, I., Zweiri, Y., 2020. Multirotors from takeoff to real-time full identification using the modified relay feedback test and deep neural networks. arXiv preprint arXiv:2010.02645 .

[5] Bangura, M., 2017. Aerodynamics and Control of Quadrotors. Ph.D. thesis.

[6] Boiko, I., 2012. Non-parametric Tuning of PID Controllers: A Modified Relay-Feedback-Test Approach. Advances in Industrial Control, Springer London.

[7] Boiko, I., 2013. Modified relay feedback test (mrft) and tuning of pid controllers, in: Non-parametric Tuning of PID Controllers: A Modified Relay-Feedback-Test Approach. Springer London, London, pp. 25–79.

[8] Bry, A., Richter, C., Bachrach, A., Roy, N., 2015. Aggressive flight of fixed-wing and quadrotor aircraft in dense indoor environments. The International Journal of Robotics Research 34, 969–1002.

[9] Chehadeh, M.S., Boiko, I., 2019. Design of rules for in-flight non-parametric tuning of PID controllers for unmanned aerial vehicles. Journal of the Franklin Institute 356, 474–491.

[10] Chéron, C., Dennis, A., Semerjyan, V., Chen, Y., 2010. A multi-functional hil testbed for multirotor vtol uav actuator, in: Proceedings of 2010 IEEE/ASME International Conference on Mechatronic and Embedded Systems and Applications, pp. 44–48.

[11] Faessler, M., Franchi, A., Scaramuzza, D., 2018. Differential flatness of quadrotor dynamics subject to rotor drag for accurate tracking of high-speed trajectories. IEEE Robotics and Automation Letters 3, 620–626.

[12] Guo, K., Jia, J., Yu, X., Guo, L., Xie, L., 2020. Multiple observers based anti-disturbance control for a quadrotor uav against payload and wind disturbances. Control Engineering Practice 102, 104560. URL: https://www.sciencedirect.com/science/article/pii/S0967066120301544, doi:https://doi.org/10.1016/j.conengprac.2020.104560.

[13] Hamandi, M., Tognon, M., Franchi, A., 2020. Direct acceleration feedback control of quadrotor aerial vehicles, in: 2020 IEEE International Conference on Robotics and Automation (ICRA), IEEE. pp. 5335–5341.

[14] Hamel, T., Mahony, R., 2006. Attitude estimation on so [3] based on direct inertial measurements, in: Proceedings 2006 IEEE International Conference on Robotics and Automation, 2006. ICRA 2006., IEEE. pp. 2170–2175.

[15] Hoffmann, G., Huang, H., Waslander, S., Tomlin, C., 2007. Quadrotor helicopter flight dynamics and control: Theory and experiment, in: AIAA guidance, navigation and control conference and exhibit, p. 6461.

[16] Lieret, M., Lukas, J., Nikol, M., Franke, J., 2020. A lightweight, low-cost and self-diagnosing mechatronic jaw gripper for the aerial picking with unmanned aerial vehicles. Procedia Manufacturing 51, 424–430. 30th International Conference on Flexible Automation and Intelligent Manufacturing (FAIM2021).

[17] Madgwick, S., Harrison, A., Vaidyanathan, R., 2011. Estimation of imu and marg orientation using a gradient descent algorithm. IEEE ... International Conference on Rehabilitation Robotics : [proceedings] 2011, 5975346.

[18] MATLAB, 2020. Matlab optimization toolbox. The MathWorks, Natick, MA, USA.

[19] Mellinger, D., Kumar, V., 2011. Minimum snap trajectory generation and control for quadrotors, in: 2011 IEEE International Conference on Robotics and Automation, pp. 2520–2525.

[20] Mogili, U.R., Deepak, B.B.V.L., 2018. Review on application of drone systems in precision agriculture. Procedia Computer Science 133, 502–509. International Conference on Robotics and Smart Manufacturing (RoSMa2018).

[21] Mohta, K., Watterson, M., Mulgaonkar, Y., Liu, S., Qu, C., Makineni, A., Saulnier, K., Sun, K., Zhu, A., Delmerico, J., et al., 2018. Fast, autonomous flight in gps-denied and cluttered environments. Journal of Field Robotics 35, 101–120.

[22] Murali, V., Spasojevic, I., Guerra, W., Karaman, S., 2019. Perception-aware trajectory generation for aggressive quadrotor flight using differential flatness, in: 2019 American Control Conference (ACC), IEEE. pp. 3936–3943.

[23] Nekoukar, V., Mahdian Dehkordi, N., 2021. Robust path tracking of a quadrotor using adaptive fuzzy terminal sliding mode control. Control Engineering Practice 110, 104763. URL: https://www.sciencedirect.com/science/article/pii/S096706612100040X, doi:https://doi.org/10.1016/j.conengprac.2021.104763.

[24] O'Connell, M., Shi, G., Shi, X., Chung, S.J., 2021. Meta-learning-based robust adaptive flight control under uncertain wind conditions. arXiv preprint arXiv:2103.01932 .

[25] Perez, A., Wagner, J., Burggräf, P., Roth, H., 2019. Quadrotors in factory applications: design and implementation of the quadrotor's p-pid cascade control system modeling and implementation. SN Applied Sciences 1.

[26] Pounds, P., Mahony, R., Corke, P., 2010. Modelling and control of a large quadrotor robot. Control Engineering Practice 18, 691–699.

[27] Rohrer, R., Sobral, M., 1965. Sensitivity considerations in optimal system design. IEEE Transactions on Automatic Control 10, 43–48.

[28] Schoellig, A.P., Mueller, F.L., Raffaello D'andrea, ·., Schoellig, A.P., Mueller, F.L., D'andrea, ·.R., D'andrea, R., 2012. Optimization-based iterative learning for precise quadrocopter trajectory tracking 33, 103–127.

[29] Spitzer, A., Michael, N., 2019. Inverting learned dynamics models for aggressive multirotor control. arXiv preprint arXiv:1905.13441 .

[30] Tal, E., Karaman, S., 2020. Accurate tracking of aggressive quadrotor trajectories using incremental nonlinear dynamic inversion and differential flatness. IEEE Transactions on Control Systems Technology , 1–16.

[31] Torrente, G., Kaufmann, E., Foehn, P., Scaramuzza, D., 2021a. Data-driven mpc for quadrotors. arXiv:2102.05773.

[32] Torrente, G., Kaufmann, E., Föhn, P., Scaramuzza, D., 2021b. Data-driven mpc for quadrotors. IEEE Robotics and Automation Letters 6, 3769–3776.

[33] Waibel, M., Keays, B., Augugliaro, F., 2017. Drone shows: Creative potential and best practices. Technical Report. Zürich.

[34] Zhang, H., Sun, J., Zhao, J., 2019. Compliant bistable gripper for aerial perching and grasping, pp. 1248–1253.